# Global simulation of magnetosonic wave instability in the storm time magnetosphere

Lunjin Chen,[1] Richard M. Thorne,[1] Vania K. Jordanova,[2] and Richard B. Horne[3]

[1]   Coupling between the Rice Convection Model and Ring Current–Atmospheric Interactions Model codes is used to simulate the dynamical evolution of ring current ion phase space density and the thermal electron density distribution for the 22 April 2001 storm. The simulation demonstrates that proton ring distributions ($df_\perp/dv_\perp > 0$) develop over a broad spatial region during the storm main phase, leading to the instability of equatorial magnetosonic waves. Calculations of the convective growth rate of magnetosonic waves for multiples of the proton gyrofrequency from 2 to 42 are performed globally. We find that the ratio between the perpendicular ring velocity and the equatorial Alfven speed determines the frequency range of unstable magnetosonic waves. Low harmonic waves ($\omega < 10\ \Omega_{H^+}$) tend to be excited in the high-density nightside plasmasphere and within the duskside plume, whereas higher-frequency waves ($\omega > 20\ \Omega_{H^+}$) are excited over a broad spatial region of low density outside the morningside plasmasphere.

## 1.   Introduction

[2]   Fast magnetosonic (MS) waves, also called equatorial noise, at frequencies from a few to several hundreds of hertz, are primarily observed within ~2°–3° of the geomagnetic equator [*Russell et al.*, 1970; *Santolík et al.*, 2002; *Němec et al.*, 2005] both inside and outside the plasmapause. Early observation studies [e.g., *Perraut et al.*, 1982] demonstrated that MS waves occur as a series of narrow tones, spaced at multiples of the proton gyrofrequency up to the lower hybrid resonance frequency $f_{LHR}$. It has been suggested [*Curtis and Wu*, 1979; *Boardsen et al.*, 1992; *Horne et al.*, 2000] that such equatorial MS waves are excited at very oblique wave normal angles by a natural instability associated with a ring distribution ($\partial f/\partial v_\perp > 0$) of energetic protons at energies of the order of 10 keV and with the velocity of the peak phase space density exceeding the local Alfvenic speed. A recent survey [*Meredith et al.*, 2008] of wave and particle data from the Combined Release and Radiation Effects Satellite (CRRES) confirmed the role of proton rings as a potential source mechanism.

[3]   Equatorial MS waves can also influence radiation belts dynamics during active periods, leading to local electron acceleration from ~10 keV up to a few MeV in the

outer radiation belts [*Horne et al.*, 2007]. For the strongest MS waves, the acceleration time scale of 1–2 days via electron Landau resonance is comparable to that due to whistler mode chorus waves [e.g., *Horne et al.*, 2005; *Li et al.*, 2007]. Furthermore, owing to the equatorial spatial confinement, energetic electrons in the outer radiation belt can be subject to nonresonant transit time scattering, in addition to the Landau resonant scattering predicted by quasi-linear theory [*Bortnik and Thorne*, 2010].

[4]   Global ring current simulations have previously been used to study the excitation of whistler mode chorus [*Jordanova et al.*, 2010] and electromagnetic ion cyclotron (EMIC) waves [*Jordanova et al.*, 2001; *Chen et al.*, 2010], both of which are of importance in radiation belts dynamics. However, no comparable simulation has been made of the global excitation and expected frequency distribution of equatorial MS waves. In addition, there has been no systematic analysis of how variations in the Alfvénic speed affect MS wave excitation. Consequently, in this study a global simulation of ring current ion dynamics will be used to evaluate the spatial distribution of MS wave convective growth rate as a function of wave frequency, and also investigate the role of Alfvén speed variation in the MS wave growth. A brief description of how coupling between the Rice Convection Model (RCM) and the Ring current-Atmospheric interactions Model (RAM) is used to simulate the dynamical evolution of thermal (~eV) electron plasma density and energetic ions phase space density in the inner magnetosphere, is presented in section 2. The results of the coupled RCM and RAM simulation for the 22 April 2001 storm are presented in section 3, with an emphasis on the global development of proton ring distributions during the

[1]Department of Atmospheric Sciences, University of California, Los Angeles, California, USA.
[2]Los Alamos National Laboratory, Los Alamos, New Mexico, USA.
[3]British Antarctic Survey, Natural Environment Research Council, Cambridge, UK.

storm main phase. A theoretical analysis of MS wave instability is given in section 4 and Appendices A and B. The simulated ion distributions are utilized for calculating the convective growth rate of MS waves globally in section 5. Finally, we summarize our principal conclusions and discuss the need for further analysis of resonant scattering by excited waves, and describe pertinent observational test for our predictions.

## 2. Coupled Model of Ring Current Ion Dynamics

[5] A global simulation of energetic ring current ion and electron phase space density, and thermal electron plasma density distribution, has been performed by coupling of two well-established codes: RCM [*Toffoletto et al.*, 2003, and reference within] and RAM [*Jordanova et al.*, 1996, 1997, and reference within]. The combined model has previously been described elsewhere [*Jordanova et al.*, 2010; *Chen et al.*, 2010]. The dynamic evolution of the energetic ring current ion population provides a source of free energy for the excitation of both EMIC waves [*Chen et al.*, 2010] and MS waves, and the energetic electron population can excite whistler mode chorus waves [*Jordanova et al.*, 2010]. The thermal electron density plays an important role in wave excitation by changing the resonant energy for energetic protons or electrons and by affecting the wave dispersion relationship.

[6] The RCM is an established physical model of the middle magnetosphere and plasma sheet that includes coupling to the ionosphere, by using a multifluid formalism to describe adiabatically drifting isotropic particle distributions in a self-consistently computed electric field and a specified magnetic field. The Tsyganenko 96 (T96) magnetic field model [*Tsyganenko*, 1995, 1996] is used for this study. The RCM is used to treat the transport of ions and electrons into the inner magnetosphere from the distant plasma sheet, modeling the proton and electron energy spectra with isotropic particle velocity space distributions for both species. The RCM's outer boundary is set at $\sim 20\ R_E$, and the proton and electron energy spectra at the boundary is established as a function of MLT and interplanetary conditions, based on analysis of 11 years (1995–2005) of Geotail LEP electron and ion fluxes from $\sim 0.04$ to 40 keV data and the Geotail EPIC ion data (46–3000 keV) assuming all ions are protons [*Wang et al.*, 2007; *Gkioulidou et al.*, 2009]. The time-dependent cross polar cap potential drop ($\Delta\Phi_{PCP}$) and the $Z$ component of interplanetary magnetic field (IMF $B_z$) are used as inputs for both the outer particle boundary condition and for the T96 model. To establish the initial condition for the RCM, we first ran the simulation under a time-independent $\Delta\Phi_{PCP}$ of 30 kV with quiet time T96 fields (IMF $B_z = 0$ nT) until it reached a steady state. This steady state is used as the initial condition.

[7] The energy spectrum modeled by the RCM at geosynchronous orbit ($\sim 6.6\ R_E$) is used to derive the energetic particle distribution function at the outer nightside boundary condition (or source population) for the RAM simulation. Since the RCM assumes isotropic particle distributions for both electrons and protons, the ion composition and pitch angle anisotropy of ring current ions at this outer boundary is inferred from empirical studies as a function of solar and

geomagnetic activity [*Young et al.*, 1982; *Roeder et al.*, 2005]. Subsequently, the RAM code solves fundamental kinetic equations to simulate the evolution of the distribution function of ring current electrons and ions, including $H^+$, $He^+$, and $O^+$ with energy from 500 eV to 400 keV, in the inner magnetosphere $2.0 \le L \le 6.5$. The RAM simulation takes into account various loss and transport processes including charge exchange, Coulomb collisions, atmospheric loss, escape from magnetopause, convective transport, gradient drifting, and radial diffusion. The RAM code is coupled with a plasma-spheric model [*Rasmussen et al.*, 1993] that was developed further to use an arbitrary electric field by *Jordanova et al.* [2006]. Therefore the electric field output from the RCM is used to drive both the plasmaspheric density model and the convective transport of ring current ions.

## 3. Storm Time Simulation

[8] The RAM code was used to simulate ring current species evolution in the inner magnetosphere during the 22 April 2001 storm for a 72 h period, with $t = 0$ h defined as 0000 UT on 21 April. This storm was studied extensively in the past [e.g., *Jordanova et al.*, 2010; *Chen et al.*, 2010]. An interval close to *Dst* minimum ($t = 40$ h) has been selected to evaluate the global distribution of magnetosonic waves in this study. The modeled thermal electron density distribution at this time is shown in Figure 1. A sharp plasmapause forms on the nightside (inside $L = 4$) and an extended high-density plume forms in the afternoon sector. Dayside refilling from the ionosphere tends to increase the electron content on the dayside. The modeled thermal electron density ($n_e$) is used to calculate the Alfvénic speed $V_A = B(\mu_0 n_e m_{H^+})^{-(1/2)}$, where $m_{H^+}$ is the proton mass, and also evaluate the phase speed of magnetosonic waves assuming a cold plasma dispersion relationship for a proton-electron plasma under the assumption of a dipole magnetic field **B**.

[9] Energetic proton phase space density (PSD), *f*, is obtained from the RAM code and examples of the PSD at $L = 5$ in 3 h MLT intervals are shown in Figure 2. At this $L$ shell, the PSD within $\sim 3$ h of midnight is essentially bi-Maxwellian with a loss cone feature of a few degrees and perpendicular temperature greater than parallel temperature (Figures 2c, 2e, and 2h), as a consequence of inward convective injection on the nightside. Proton ring-like distributions, with a pronounced peak along the $v_\perp$ axis at $\sim 10$ keV to a few tens of keV, occur from the dusk sector to the morning sector (Figures 2a, 2d, 2f, and 2g), as a result of energy-dependent drifting and loss. Ring current protons of intermediate energy ($\sim$a few keV, or velocity comparable to $V_{dip}$ as schematically illustrated in Figure 2, center) have little access to these locations. Protons above 10 keV are predominately subject to westward magnetic gradient drifting, while the motion of protons less than several keV are dominated by electric field drift in the eastward direction from nightside injection, extending to the noon sector.

[10] To describe the characteristics of these proton rings, the properties of the PSD along the $v_\perp$ axis, $f_\perp(v_\perp) \equiv f(v_\perp, v_\parallel = 0)$, are investigated. As shown in Figure 2 (center), the velocity $v_\perp$ of the $f_\perp$ peak is called the ring velocity $V_R$, while the $v_\perp$ of the PSD minimum below $V_R$ is called the dip velocity $V_{dip}$. If no minima are found, $V_{dip}$ is set to the lower velocity limit in
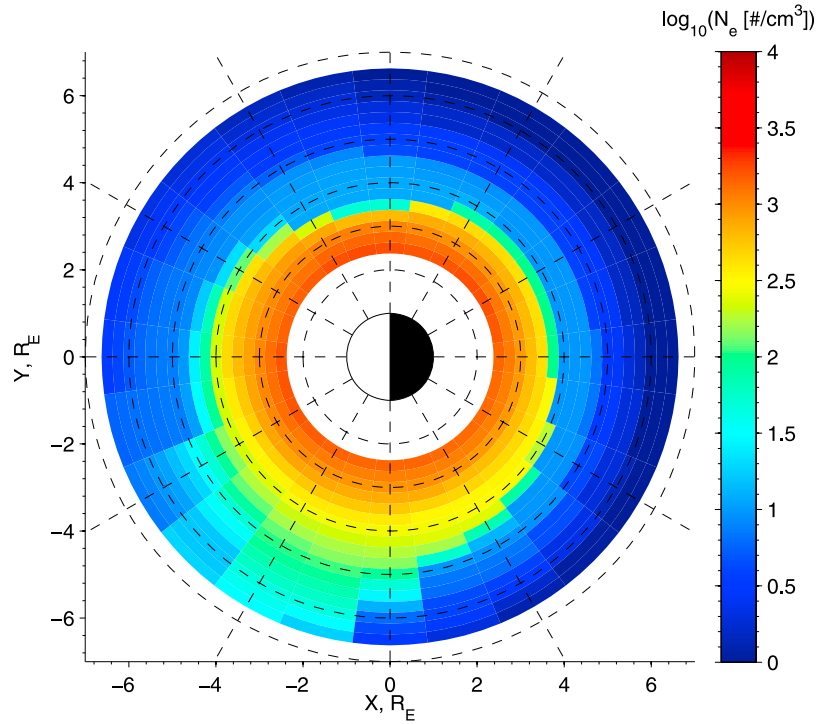
**Figure 1.** Simulation of thermal electron density distribution for the 22 April 2001 storm during the main phase ($t$ = 40 h).

the simulation domain. Correspondingly, the ring energy is defined as $E_R = \frac{1}{2}m_{H^+}V_R^2$, the dip energy $E_{\text{dip}} = \frac{1}{2}m_{H^+}V_{\text{dip}}^2$, and the Alfvén energy $E_A = \frac{1}{2}m_{H^+}V_R^2$ ($=B^2(2\mu_0 n_e)^{-1}$).

[11] These proton rings, with positive $df_\perp/dv_\perp$ in the $v_\perp$ range between $V_{\text{dip}}$ and $V_R$, provide a source of free energy for exciting MS waves. Conversely, negative $df_\perp/dv_\perp$ above $V_R$ or below $V_{\text{dip}}$ contributes to wave damping. Generally, the relative contribution for growth or damping from different portions of phase space must be considered to determine the net growth or damping of MS waves. Therefore it is helpful to identify the spatial locations of proton rings and to investigate the characteristics of these proton rings (the properties of the function $f_\perp(v_\perp)$).

[12] Proton rings are identified by the following three criteria: (1) A clear peak of $f_\perp$ exists (thus $V_R$ exists); (2) the phase space density of the peak is significant, $f_\perp(v_\perp = V_R) \geq 5 \times 10^{-15}$ m$^{-6}$ s$^3$, which is comparable to that of *Horne et al.* [2000, Figure 2]; and (3) the peak is well pronounced, $f_\perp(v_\perp = V_R)/f_\perp(v_\perp = V_{\text{dip}}) \geq 2$. The global distribution of easily identifiable rings is shown in the colored areas in Figure 3. The quantities $f_\perp(v_\perp = V_R)$, $V_R/V_A$, $E_R$, and $E_{\text{dip}}$ are color-coded in Figures 3a, 3b, 3c, and 3d, respectively. Proton rings are present over a broad spatial region from inside the plamasphere at night, through the plume in the afternoon, to both inside and outside the plasmasphere in the morning sector. The ring energy ranges from a few to a few tens of keV, while the dip energy is comparable to a few keV. Ring PSD $f_\perp(v_\perp = V_R)$ increases at later MLT and larger $L$ with an accompanying decrease in $E_R$ and $E_{\text{dip}}$. The ratio $V_R/V_A$ varies from a few tenths up to 4, with a tendency to maximize in the high-density region, just inside

the plamaspause on the dayside and inside the plume in the afternoon sector (Figure 3b).

## 4. Theoretical Instability Analysis

[13] The general nonrelativistic condition for resonant interaction between magnetosonic waves and protons is

$$\omega - k_\parallel v_{res\parallel} = m\Omega_{H^+}, \qquad (1)$$

where $\omega$ is the MS wave frequency, $k_\parallel$ the component of the wave vector **k** along the direction of the ambient magnetic field **B**, $m$ is an integer representing the order of cyclotron harmonics resonance, $\Omega_{H^+}$ is the proton gyro frequency, and $v_{res\parallel}$ is the proton parallel resonant velocity. For field-aligned waves, only $m = -1$ or $+1$ resonant interactions are relevant for R mode and L mode, respectively. However, for MS waves with highly oblique wave normal angle, multiple resonant interactions, including Landau resonance ($m = 0$), become important.

[14] For small temporal growth rate $\gamma \ll \omega$, $\gamma$ can be expressed explicitly as the summation of the contributions from every harmonic resonant interaction with resonant particles [e.g., *Kennel*, 1966; *Chen et al.*, 2010]. MS waves are essentially the low-frequency extension of whistler mode waves with wave normal angle $\theta$ close to 90°. These waves are capable of propagating in the inhomogeneous magnetosphere in both the radial and azimuthal directions [e.g., *Kasahara et al.*, 1994]. To evaluate net wave gain along the wave raypath, it is more convenient to calculate the convective growth rate $k_i$, the imaginary part of the complex wave vector. In fact, it is the component $K_i$ of $\mathbf{k}_i$
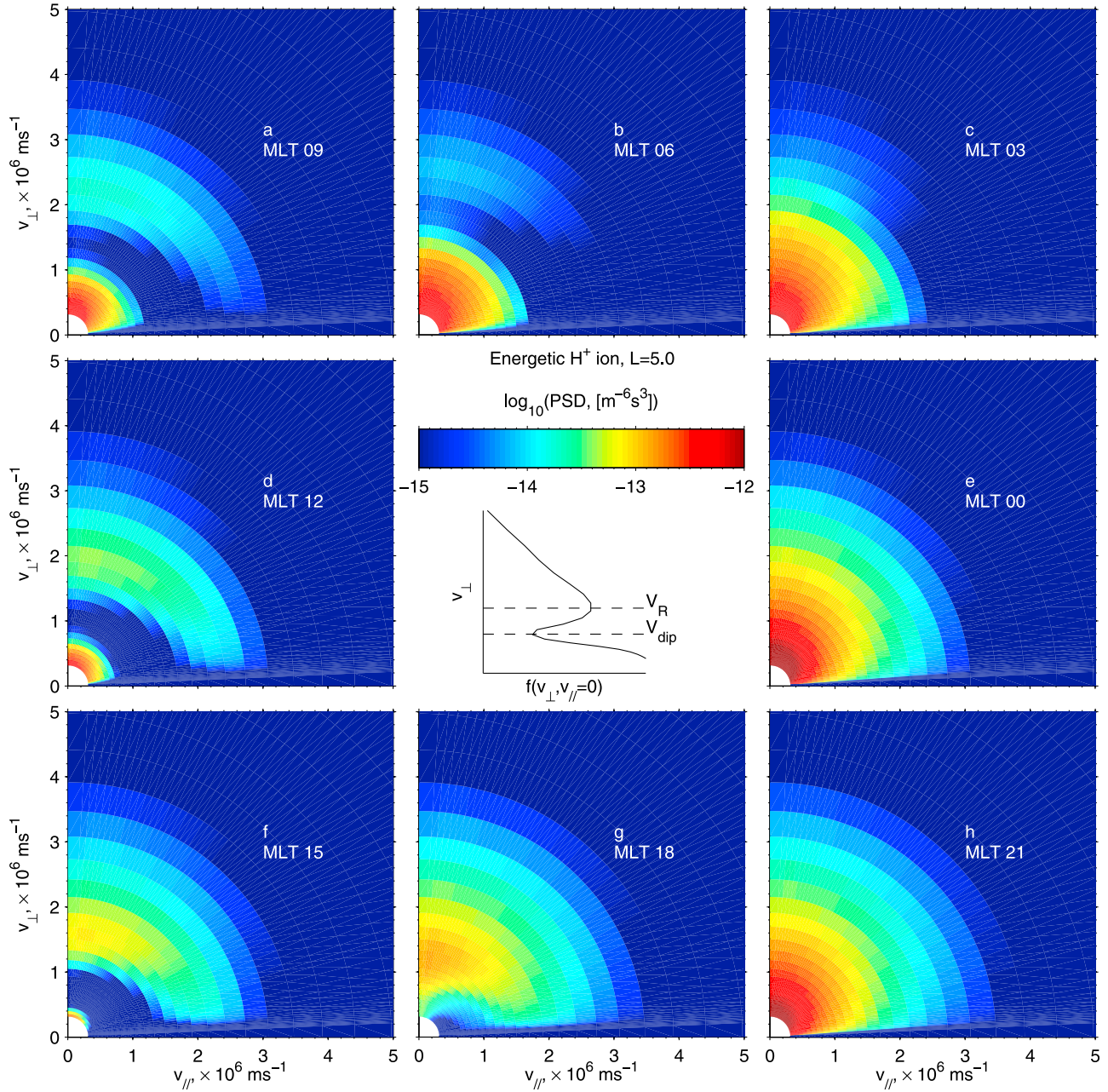
**Figure 2.** Simulation of energetic proton phase space density $f(v_\perp, v_\parallel)$ at $L = 5$ in 3 h MLT intervals for $t = 40$ h. The center shows a schematic profile of ring-like PSD along the $v_\perp$ axis (solid line), with the ring velocity $V_R$ and the dip velocity $V_{\text{dip}}$ (dashed horizontal lines).

along the group velocity $\mathbf{v}_g$ that matters, because of the pronounced anisotropy of the wave refractive index surface for MS waves.

[15] As shown in Appendix A, $K_i$ can be expressed as

$$K_i = \sum_{m=-\infty}^{+\infty} \int_0^\infty dv_\perp \left( W_{m,\perp} \frac{\partial f}{\partial v_\perp} + W_{m,\parallel} \frac{\partial f}{\partial v_\parallel} \right)\Big|_{v_\parallel = v_{res\parallel}}, \quad (2)$$

where positive (or negative) $K_i$ corresponds to growth (or damping), $W_{m,\perp}$ and $W_{m,\parallel}$ are perpendicular and parallel weighting functions, respectively, for harmonic resonance of order $m$. The summation is done over $m$ from $-100$ to $100$. Each term in equation (2) involves an integration over $v_\perp$,

along the resonant parallel velocity, of the product of weighting functions and the derivatives of phase space density with respect to $v_\parallel$ or $v_\perp$.

[16] These weighting functions depend on $v_\perp$ and $v_\parallel$, the order of harmonic resonance, the background cold plasma density, and the ambient magnetic field, as well as wave frequency $\omega$, wave normal angle $\theta$, and wave refractive index $n$. The PSD derivatives are determined by the velocity space distribution of energetic resonant protons. The wave refractive index is obtained through the cold plasma dispersion relation, assuming that the plasma consists only of electrons and protons and is dominated by cold species with a dilute hot proton species.
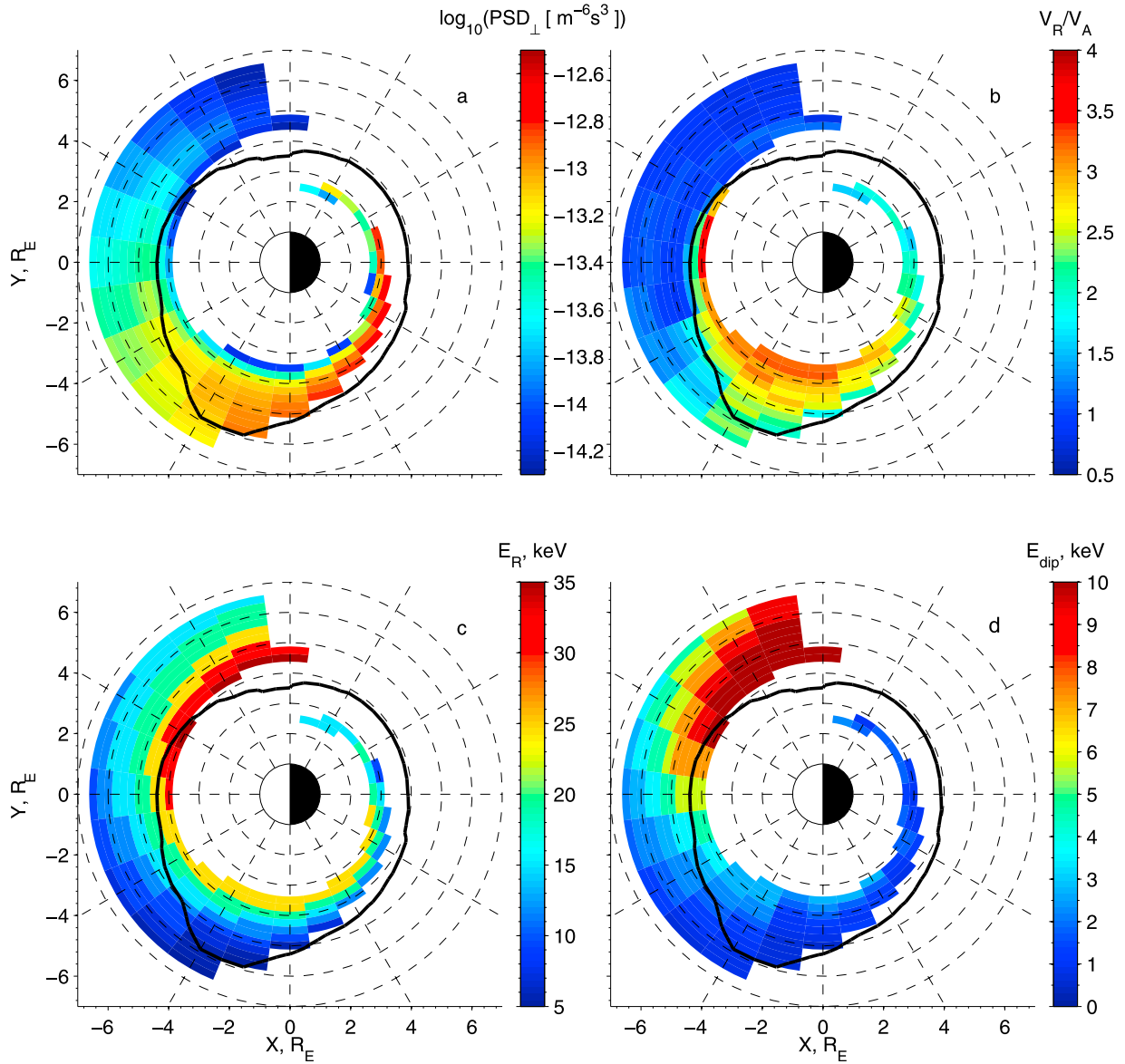
**Figure 3.** Characteristics of proton ring distribution for $t = 40$ h. The colored area, identical in Figures 3a–3d, is the region where the ring is clearly identified using the criteria described in the text. (a) The PSD peak along the $v_\perp$ axis; (b) the ratio of the ring velocity to the Alfvenic speed $V_R/V_A$; (c) ring energy $E_R = \frac{1}{2}m_{H^+}V_R^2$, and (d) dip energy $E_{dip} = \frac{1}{2}m_{H^+}V_{dip}^2$. Black solid lines denote the 50 cm$^{-3}$ contour of the thermal electron density.

[17] In the present study, we focus on examining waves with nearly perpendicular propagation (wave normal angle $\theta = 89.5°$) at exact multiples of the proton gyrofrequency $\omega = m_\omega\Omega_{H^+}$, where $m_\omega$ is an integer $2 \leq m_\omega < \omega_{LHR}/\Omega_{H^+}$ and $\omega_{LHR}$ is the lower hybrid resonance frequency. The choice of this wave normal angle is motivated by the earlier analysis by *Horne et al.* [2000], who suggested that the electron Landau damping by plasma sheet electrons suppresses to a large extent MS waves with small wave normal angle (<85°) and thus restricts propagation to angles close to perpendicular to the magnetic field. When propagation characteristics are considered, the most unstable MS waves occur at a wave normal angle 89.5° [*Horne et al.*, 2000, Figure 9]. On the basis of our growth rate calculation, we find that the unstable frequency range of MS waves is not sensitive to the choice of the wave normal angle when wave normal angle is greater than 89° (not shown here). The growth rate calculation is done by ignoring the electron Landau damping for the following two reasons: (1) The electron Landau damping rate is small for MS waves with almost perpendicular propagation >89°, which requires high Landau resonant energy (>~keV), and (2) the electron Landau damping rate is much less than the growth rate of MS waves due to unstable proton rings from our simulation, where no wave-induced relaxation is included.

[18] It follows from equation (1) that the proton resonant energy for harmonic resonance of order $m$, $E_{res\parallel} = (m_\omega - m)^2 E_0$ where $E_0 = \frac{1}{2}m_{H^+}(\omega/k_\perp)^2(\tan\theta/m_\omega)^2$. For
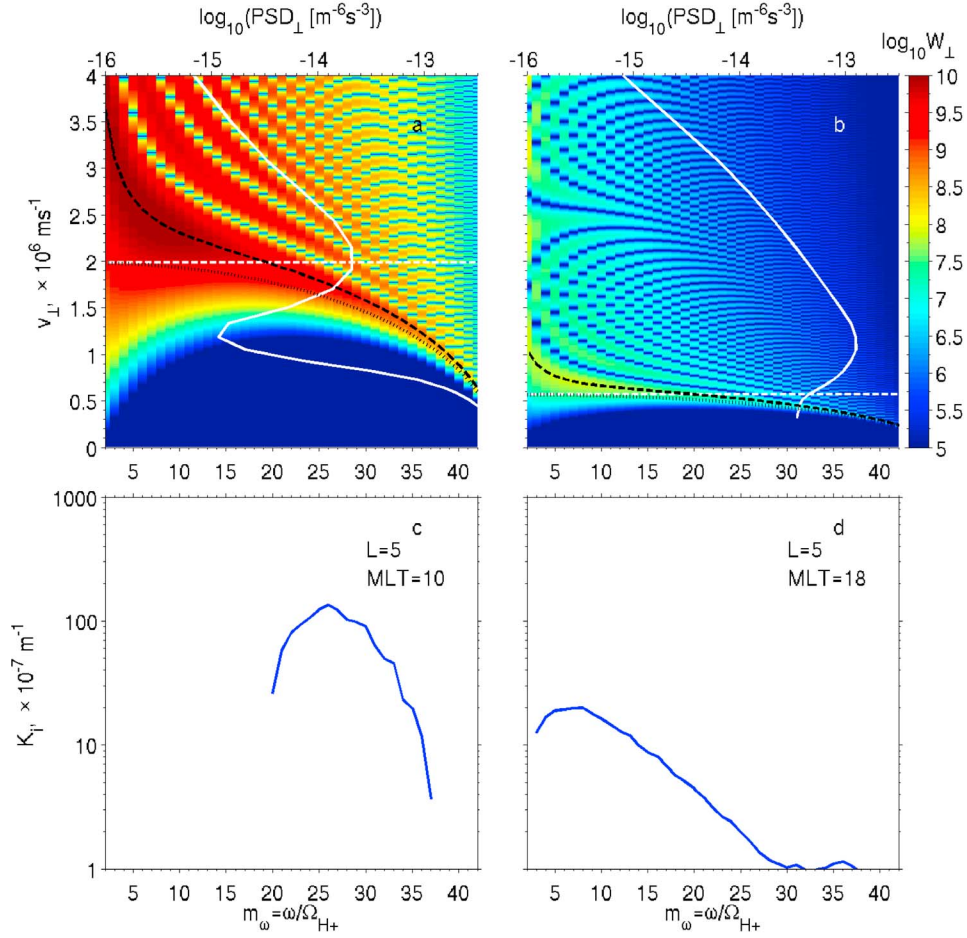
**Figure 4.** (a) Weighting function $W_\perp$ as a function of $v_\perp$ and $m_\omega = \omega/\Omega_{H+}$, in a low-density region outside the plasmasphere, $L = 5$ and MLT = 10. The energetic proton PSD along the $v_\perp$ axis is shown as a solid white line. The dashed horizontal white line represents the local Alfvénic speed $V_A$, the dashed black line is $v^*_{\perp\text{peak}}$ (the $v_\perp$ of peak $W_\perp$), and the dotted black line is the perpendicular phase speed of MS waves $\omega/k_\perp$. (c) The component of corresponding local convective growth rate along the group velocity, $K_i$, as a function of $\omega/\Omega_{H+}$. (b and d) Same as in Figures 4a and 4b except for another location, $L = 5$ and MLT = 18 inside the plume.

small $m_\omega$ ($\leq$20 and $\omega/k_\perp \approx V_A$), only a single resonance of order $m = m_\omega$ contributes to $K_i$ with zero parallel resonant energy; since the lowest minimum resonant energy among the other resonances, $m = m_\omega \pm 1$, is comparable to $(10^2 - 10^3)$ $E_A$, where few protons are present and the corresponding gradients $\partial f/\partial \mathbf{v}$ are small. At larger $m_\omega$, $(\tan\theta/m_\omega)^2$ decreases and $\omega/k_\perp$ drops as $\omega$ approaches $\omega_{\text{LHR}}$, leading to significant contribution from harmonic resonance other than $m_\omega$ as well. However, the $m = m_\omega$ resonance is still dominant because of the larger number of resonant protons at zero parallel velocity, since the proton phase space density generally peaks around pitch angle $\alpha = 90°$ (Figure 2). Consequently, one may better understand the dominant physical processes which lead to wave excitation using a semiquantitative analysis, in which $K_i$ can be approximated (see Appendix B) as

$$K_i \approx \int_0^\infty dv_\perp \left( W_\perp \frac{\partial f}{\partial v_\perp} \right)\Big|_{v_\parallel=0}, \qquad (3)$$

where $W_\perp$ is the perpendicular weighting function of harmonics resonance of order $m = m_\omega$ and the $\partial f/\partial v_\parallel$ term vanishes at $v_\parallel = 0$. It should be noted that the above approximated expression of $K_i$ is used only for analyzing the physical condition of MS wave instability and the calculation of the growth rate $K_i$ is done precisely using the equation (2) throughout the present study. It is also shown in Appendix B that $W_\perp$ is proportional to $J^2_{m_\omega}$ for most $m_\omega$ of interest, where $J_{m_\omega}$ is a Bessel function of order $m_\omega$ and argument $x = k_\perp v_\perp/\Omega_{H+}$. The velocity $v_\perp$ of the $W_\perp$ peak can be approximated as $v^*_{\perp\text{peak}} = \zeta\omega/k_\perp$ (see derivation in Appendix B). The $\zeta \sim 1.6$ at $m_\omega = 3$, and monotonically approaches to 1 as $m_\omega$ increases. The perpendicular phase velocity $\omega/k_\perp$ (equation (B9)) is comparable to $V_A$ but decreases at higher frequency as $\omega$ approaches $\omega_{\text{LHR}}$. Consequently, $v^*_{\perp\text{peak}}$ is in the vicinity of $V_A$ for $m_\omega < 25$ (1.6 $V_A$ for $m_\omega = 3$ and $V_A$ for $m_\omega = 20$), and decreases monotonically as $\omega$ approaches $\omega_{\text{LHR}}$.

[19] Figure 4a shows an example of $W_\perp$ as a function of $v_\perp$ and $m_\omega = \omega/\Omega_{H+}$ at the location $L = 5$, MLT = 10. Oscillations

of $W_\perp(v_\perp)$ for fixed $m_\omega$ are related to the properties of the Bessel functions. The values of $v^*_{\perp\text{peak}}$, the dominant peak in $W_\perp(v_\perp)$, and the perpendicular wave phase speed $v_{\perp\text{ph}}(=\omega/k_\perp)$ are indicated as a function of $m_\omega$ by black dashed and dotted lines, respectively. The perpendicular phase speed is approximately the Alfven speed $V_A$ (Figure 4a, white horizontal dashed line) for $\omega/\Omega_{H^+} < 10$, but decreases monotonically as $\omega/\Omega_{H^+}$ increases and drops dramatically as $\omega$ approaches $\omega_{LHR}$. Note that the approximation $v^*_{\perp\text{peak}}$ agrees well with the first predominant peak of the exact value of $W_\perp$. The $v^*_{\perp\text{peak}}$ decreases monotonically and crosses $V_A$ at $\omega \sim 20\ \Omega_{H^+}$. The $v_\perp$ range of proton PSD near $v^*_{\perp\text{peak}}$ contributes the most to $K_i$. Consequently, as a rule of thumb, instability of MS waves at any specified frequency can be determined by the sign of the derivative of phase space density $\partial f/\partial v_\perp$ along $v_\parallel = 0$ near $v_\perp = v^*_{\perp\text{peak}}$. Waves are unstable (or stable) when the derivative is positive (or negative). Figure 4c shows the convective growth rate of MS waves, $K_i$ given by equation (2) with all the harmonic resonance contributions (all $m$), as a function of the wave frequency normalized to the proton gyrofrequency ($2 \leq m_\omega \leq 42$). At this location, $V_R/V_A \sim 1$. Instability occurs over the frequency range $20 \leq m_\omega \leq 36$, where the $v^*_{\perp\text{peak}}$ lies in the positive $df_\perp/dv_\perp$ range. Peak growth rate ($\sim 10^{-5}$ m$^{-1}$) occurs at a wave frequency $\sim 26\ \Omega_{H+}$; the corresponding value of $v^*_{\perp\text{peak}}$ lies just below $V_R$, where the $df_\perp/dv_\perp$ maximizes. This peak growth rate is 2 orders of magnitude greater than that found by *Horne et al.* [2000], since the RAM simulation does not include ion relaxation process due to the wave-particle scattering. Such scattering will reduce the gradients and consequently lead to smaller wave growth. The simulated MS wave growth rate spectrum also shows sharp cutoffs at each end of the unstable frequency band. The waves with frequencies greater than $36\ \Omega_{H^+}$ are damped predominately because of negative $df_\perp/dv_\perp$ above the ring energy $E_R$, while those with frequencies less than $20\ \Omega_{H^+}$ are predominantly damped by the presence of negative $df_\perp/dv_\perp$ below $E_{\text{dip}}$. Therefore the value of $V_R$ and $V_{\text{dip}}$ with respect to $V_A$ can be used to predict the wave frequency range of instability. The $df_\perp/dv_\perp$ above $E_R$ (or below $E_{\text{dip}}$) is responsible for damping at lower (higher) wave frequencies, respectively.

[20] A second example of instability analysis, inside the high-density plume at $L = 5$ and MLT = 18, is shown in Figures 4b and 4d. Compared with the previous case, the thermal electron density is about 1 order of magnitude greater, leading to a factor of $\sim 3$ drop in $V_A$ and about a 2 order of magnitude drop in $W_\perp$, which indicates weakening of MS wave instability in higher-density regions. Although $V_R$ decreases at later MLT, the ratio $V_R/V_A$ remains large inside the plume (>2 in this case). The instability of waves shifts toward lower wave frequencies $3 \leq m_\omega \leq \sim 30$ with the peak growth around $5 \leq m_\omega \leq 8$. Wave growth rate slowly drops at high frequencies due to absence of the pronounced low-energy component of proton PSD. Despite the presence of negative gradients over a broad range of $v_\perp$ above $V_R$, the instability can extend to as low as $3\ \Omega_{H+}$ because of the drop in $V_A$ to a value well below $V_R$, which results in positive gradients near $v^*_{\perp\text{peak}}$ for resonance at such low frequencies. The peak wave growth rate ($\sim 10^{-6}$ m$^{-1}$) is 1 order of magnitude less than that at 10 MLT outside the plume (Figure 4c). This is a consequence of the $\sim 2$ order of mag-

nitude drop in $W_\perp$, partially compensated by an $\sim 1$ order of magnitude increase in ion phase space density near the peak of the storm time ring current.

## 5. Global Instability Analysis

[21] To explore the MLT dependence of the MS wave instability, the same analysis is applied at other MLT for $L = 5$. Figure 5 shows the color-coded convective growth rate as a function of MLT and wave frequency. The MLT profile of the thermal electron density is superimposed as a dashed black line. MS instability occurs over a broad MLT range from 6 to 18, which is essentially identical to the MLT distribution of the proton rings (Figure 3). The only exception is at MLT = 6 because of the low ring PSD at MLT = 6, which is ruled out by the adopted proton ring identification criteria.

[22] Unstable MS waves outside the plume (MLT from 6 to 14) tend to occur in a higher-frequency band (>15 $\Omega_{H^+}$, centered around $\sim 30\ \Omega_{H^+}$) with a sharp drop in growth rate at both low and high frequencies; Conversely, those inside the plume occur over a broad frequency band with peak growth rate near a few $\omega/\Omega_{H^+}$. The peak growth rate inside the plume is considerably less than outside the plume.

[23] To characterize the MLT profile of typical unstable wave frequencies, the center of the unstable wave spectrum $\langle\omega\rangle_{\text{ave}}/\Omega_{H^+}$ is obtained as follows: (1) For a specified location, wave frequencies with $K_i$ greater than a critical value of $10^{-6}$ m$^{-1}$ are selected; (2) the center of the wave spectrum is defined as the median of the selected unstable wave frequencies. The MLT profile of the center of wave spectrum at $L = 5$ is plotted as a solid white line in Figure 5. The center of the wave spectrum is not identical to the peak of the wave growth rate spectrum but should represent the center of the wave power spectrum, since waves with growth rates larger than such a threshold ($10^{-6}$ m$^{-1}$) should grow to observable levels.

[24] The variation of $\langle\omega\rangle_{\text{ave}}/\Omega_{H^+}$ is strongly modulated by the ratio $V_R/V_A$, shifting toward smaller (higher) wave frequency as $V_R/V_A$ increases (or decreases). A positive slope of $\langle\omega\rangle_{\text{ave}}/\Omega_{H^+}$ versus MLT occurs in the region where $V_R/V_A$ decreases as MLT increases, including regions of relatively unchanged density (MLT 9–13) because of decreasing $V_R$ at larger MLT, and in the eastward edge of the plume (MLT 17–18) where the density decreases rapidly. A negative slope is found in regions where the density increases significantly as MLT increases: the early morning sector MLT 7–9 due to the dayside refilling from the ionosphere, and the westward edge of the plume (MLT 13–16).

[25] The instability analysis has also been performed globally and the resulting distribution of median excited wave frequencies is shown in Figure 6. The blank region represents locations where either MS waves are damped for all $m_\omega$ or the MS wave growth rate is less than $10^{-6}$ m$^{-1}$. Clearly, the normalized frequency distribution $\langle\omega\rangle_{\text{ave}}/\Omega_{H^+}$ is strongly modulated by the ratio $V_R/V_A$ (Figure 3b). High-frequency waves (>20 $\Omega_{H^+}$) are preferentially excited from the morningside to the eastward edge of the plume, over a broad spatial region $4 \leq L \leq 6.5$ outside the plasmasphere. A sharp change in the excited wave spectrum occurs at the eastward edge of the plume. Waves inside the high-density
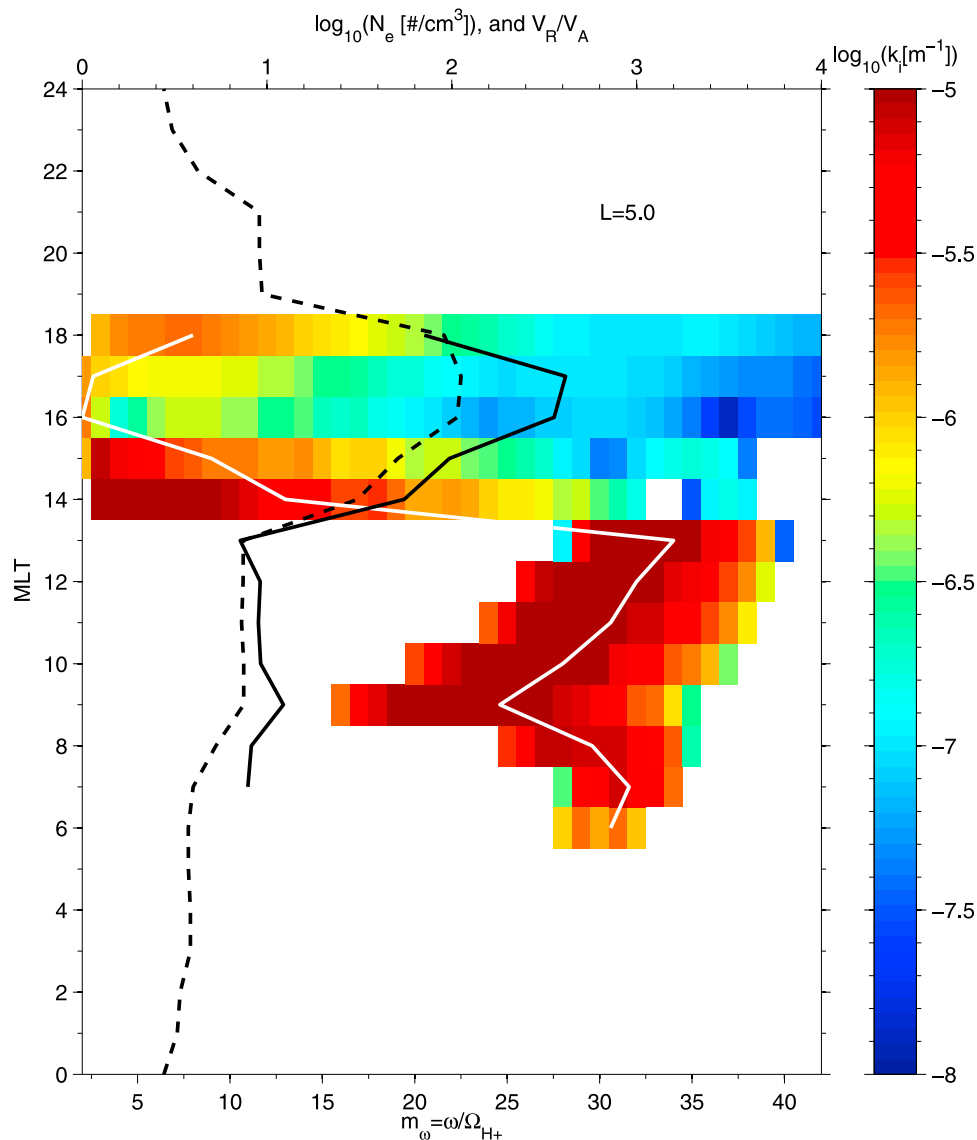
**Figure 5.** The local convective growth rate $K_i$ as a function of wave frequency and MLT at the fix $L = 5$. The dashed and solid black lines denote MLT distribution of thermal electron density and the ratio $V_R/V_A$, respectively. The center frequency of MS wave growth rate spectrum normalized to local proton gyrofrequency, $\langle\omega\rangle_{ave}/\Omega_{H^+}$, is shown in the solid white line.

plume tend to be excited at much lower wave frequency ($<10\ \Omega_{H^+}$). No waves are excited inside the high-density region in the afternoon sector where $V_R/V_A$ is greater than ~3. Such high values of $V_R/V_A$ result in the $v^*_{\perp peak}$ being far below the $V_R$ and thus small $df_\perp/dv_\perp(v_\perp = v^*_{\perp peak})$, which therefore inhibits the excitation.

## 6. Conclusions and Discussions

[26] The dynamical variability of the thermal density distribution and the injected ring current proton phase space density have been simulated by coupling the RCM and RAM codes for the 22 April 2001 storm. These modeled properties of ion phase space density during the main phase of the storm have been used to perform a global analysis of MS wave instability. Our principal conclusions are as follows:

[27] 1. Ring-type distributions of energetic protons with positive $\partial f/\partial v_\perp$ develop during the storm main phase over a broad spatial region: inside the plasmasphere at night, inside the plume on the duskside, and outside the plasmasphere in the morning sector. The presence of rings with ring velocity within a factor of 2 above or below the Alfvénic speed provides a source of free energy for MS wave excitation.

[28] 2. The center frequency of the unstable MS growth rate spectrum is strongly modulated by the ratio $V_R/V_A$. Ion ring distributions inside the high-density region (high $V_R/V_A$) from the nightside plasmasphere to the afternoon plume tend to excite MS waves with frequencies near a few $\Omega_{H^+}$, with the exception that no MS waves can be excited if $V_R/V_A$ exceeds ~3. Ion rings outside the plasmasphere (with lower $V_R/V_A$) in the morning sectors tend to excite MS waves at relatively high harmonic frequencies ($>20\ \Omega_{H^+}$).
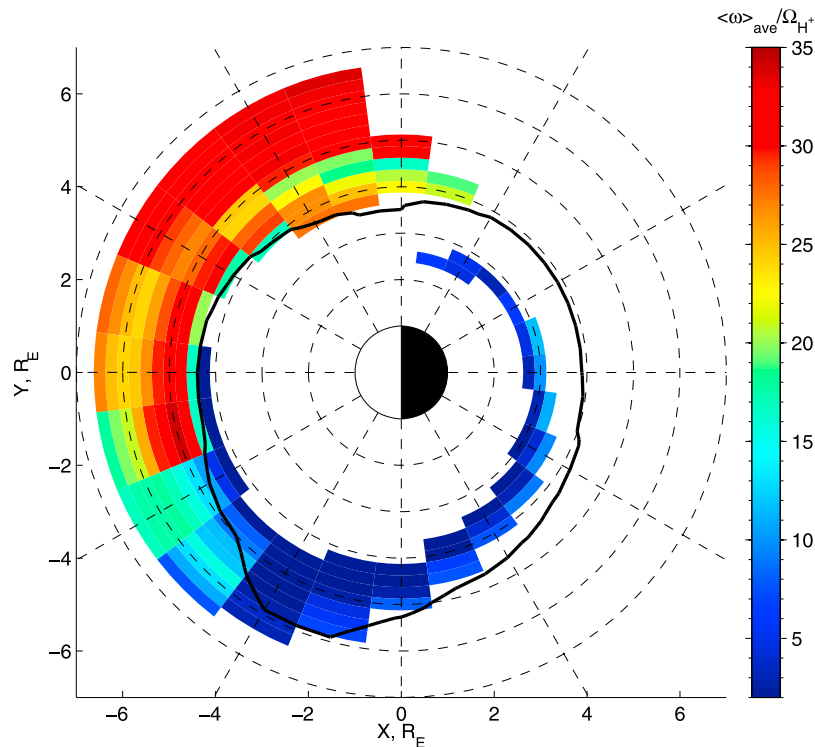
**Figure 6.** The global distribution of the center frequency of MS wave growth rate spectrum normalized to local proton gyrofrequency, $\langle\omega\rangle_{ave}/\Omega_{H^+}$. The blank region represents where the peak growth rate of MS waves is less than $10^{-6}$ m$^{-1}$. Black solid line denotes the 50 cm$^{-3}$ contour of the thermal electron density.

[29] 3. The frequency band of MS instability is bounded by low and high cutoff frequencies in the morning to noon sector outside the plasmapause. The MS waves with frequency above the high cutoff frequency is inhibited by the presence of a pronounced low-energy component (less than a few keV) below the dip energy; while those with frequency below the low cutoff are damped due to the negative gradient $df_\perp/dv_\perp$ above the proton rings.

[30] The spatial pattern of simulated proton distribution is generally consistent with the statistically spatial distribution of proton rings during active times from CRRES observations [*Meredith et al.*, 2008], namely, proton rings on the duskside inside the plamasphere and on the dayside outside the plasmasphere. One discrepancy is that proton rings are also observed outside the plasmapause at night. These proton rings could be produced by impulsive enhancement of localized convection electric field near the midnight sector, which is not included in our study. On the basis of the statistical analysis of *Meredith et al.* [2008], we find that intense MS waves are present from in the postmidnight to afternoon sector inside the plasmasphere, and over most of MLTs outside the plasmapause. Our simulated source region of MS waves agrees relatively well with the statistical observation except that in our study we do not predict MS wave instabilities from the predawn sector to the premidnight sector outside the plasmasphere. The discrepancy near midnight outside the plasmasphere might be due to the exclusion of impulsive enhancement of localized convection near midnight, which leads to the absence of unstable proton ring distribution near midnight. Also, the MS waves observed in the predawn sector outside the plasmasphere

might not be generated locally, but could originate either from MS waves observed inside the plasmasphere via radial propagation or from MS waves near midnight outside the plasmapause through azimuthal propagation.

[31] The simulated growth rate in this study is about 2 orders of magnitude higher than that predicted by *Horne et al.* [2000] based on observed ion ring distributions. This is due to the omission in the present RAM simulation of wave-particle interactions associated with scattering by the excited MS waves. Such scattering will smooth the phase space density peak associated with the proton ring distribution, and consequently reduce the growth rate of MS waves. We plan to evaluate the consequences of such quasi-linear relaxation in the future. Although the calculated growth rate in the morning sector is about 1 order of magnitude higher than that in the dusk side, this difference will be reduced when the quasi-linear scattering is included in the simulation. This scattering leads to more relaxation of those proton rings and thus more reduction of MS wave growth rate in the morning sector, because of longer transportation path over the MS wave excitation region.

[32] Only the local growth rate spectrum is shown in this study. Propagation characteristics of MS waves should also be taken into account to carefully predict the power spectrum of MS waves observed at any specified location. MS waves can propagate both radially and also azimuthally so that waves generated in one source region can contribute to the wave power at other locations. The thermal plasma density gradients will also affect the wave propagation characteristics [*Kasahara et al.*, 1994]. The waves also have the chance to be amplified multiple times when they prop-

agate through a broad source region. The growth rate of MS waves depends sensitively on wave normal angle, which will vary along the raypath [*Horne et al.*, 2000]. In the future we plan to perform 3-D path integrated wave gain in a realistic 3-D plasma density environment, to better understand the spectrum of excited MS waves.

## Appendix A: General Expression for MS Convective Growth Rate

[33] Whenever the temporal growth rate $\gamma$ is much smaller than $\omega$, we may follow *Kennel* [1966] and *Chen et al.* [2010] and reexpress the dispersion matrix $D$ to the first order as

$$D = D^{(0)} + iD_i, \tag{A1}$$

and consequently approximate

$$\gamma = -\frac{D_i}{\frac{\partial D^{(0)}}{\partial \omega}}, \tag{A2}$$

where

$$D_i = -\frac{2\pi^2 e^2}{\varepsilon_0 m_s} \frac{1}{\omega |k_\parallel|} \int_0^\infty v_\perp dv_\perp \int_{-\infty}^{+\infty} dv_\parallel \sum_m \delta\left(v_\parallel - \frac{\omega - m\Omega_s}{k_\parallel}\right)$$
$$\cdot [G_1(f_s)((P - n^2 \sin^2\theta)[2(L - n^2)v_\perp J_{m+1}^2$$
$$+ 2v_\perp(R - n^2)J_{m-1}^2 + n^2 \sin^2\theta v_\perp(J_{m+1} - J_{m-1})^2]$$
$$- n^2 \cos\theta \sin\theta[2v_\parallel J_m(J_{m+1}(R - n^2) + J_{m-1}(L - n^2))$$
$$+ n^2 \cos\theta \sin\theta v_\perp(J_{m+1} - J_{m-1})^2])$$
$$+ G_2(f_s, m)(4v_\parallel J_m[(L - n^2)(R - n^2) + n^2 \sin^2\theta(S - n^2)]$$
$$- 2n^2 \cos\theta \sin\theta[(R - n^2)v_\perp J_{m-1} + (L - n^2)v_\perp J_{m+1}])] \tag{A3}$$

where $m_s$ is mass of species $s$; $J_m$ are Bessel functions with order $m$ and argument $x = k_\perp v_\perp / \Omega_s$; $L$, $R$, $S$ and $P$ are the standard Stix coefficients; $\omega$, $\theta$, and $n = kc/\omega$ are wave frequency, wave normal angle, and refractive index,

$$G_1 = \frac{\partial f_s}{\partial v_\perp} - \frac{k_\parallel}{\omega}\left(v_\parallel \frac{\partial f_s}{\partial v_\perp} - v_\perp \frac{\partial f_s}{\partial v_\parallel}\right)$$
$$G_2 = J_m\left[\frac{\partial f_s}{\partial v_\parallel} + \frac{m\Omega}{\omega v_\perp}\left(v_\parallel \frac{\partial f_s}{\partial v_\perp} - v_\perp \frac{\partial f_s}{\partial v_\parallel}\right)\right] \tag{A4}$$
$$D^{(0)} = 4(An^4 - Bn^2 + C),$$

with $A = S \sin^2\theta + P \cos^2\theta$, $B = RL \sin^2\theta + PS(1 + \cos^2\theta)$, and $C = PRL$.

[34] Using the relation $\mathbf{k_i} \cdot \mathbf{v}_g = -\gamma$ [*Ashour-Abdalla and Kennel*, 1978; *Horne*, 1989], where

$$\mathbf{v}_g = -\frac{\partial D^{(0)}}{\partial \mathbf{k}} \bigg/ \frac{\partial D^{(0)}}{\partial \omega},$$

and assuming $\mathbf{k_i} \| \mathbf{k_r}$, the convective growth rate $k_i \equiv \mathbf{k_i} \cdot \hat{\mathbf{k}}$ can be expressed as

$$k_i = -\frac{D_i}{\hat{\mathbf{k}} \cdot \frac{\partial D^{(0)}}{\partial \mathbf{k}}} = -\frac{kD_i}{8n^2(2An^2 - B)}. \tag{A5}$$

[35] The component ($K_i$) of $\mathbf{k_i}$ along the group velocity, which leads to convective amplification along the wave raypath

$$K_i \equiv -(\hat{\mathbf{k}} \cdot \hat{\mathbf{v}}_g)k_i = \gamma/|\mathbf{v}_g|. \tag{A6}$$

The minus sign here is defined so that positive (or negative) values of $K_i$ represent the growth (or damping). Generally, $K_i$ can be expressed in an alternative way:

$$K_i = \sum_{m=-\infty}^{+\infty} \int_0^\infty dv_\perp \left(W_{m,\perp} \frac{\partial f}{\partial v_\perp} + W_{m,\parallel} \frac{\partial f}{\partial v_\parallel}\right)\big|_{v_\parallel = v_{res\parallel}}, \tag{A7}$$

where $W_{m,\perp}$ and $W_{m,\parallel}$ are the perpendicular and parallel weighting functions, respectively, for harmonic resonance of order $m$. It is straightforward to obtain the expressions for weighting functions $W_{m,\perp}$ and $W_{m,\parallel}$, from equations (A2), (A3), (A6), and (A7).

## Appendix B: A Useful Approximation for the Peak in the Weighting Function $W_\perp$

[36] In the present study, we examine instability of MS waves at multiples of the proton gyrofrequency ($\omega = m_\omega \Omega_{H^+}$, where $m_\omega$ is a whole number greater than 1), and at very oblique wave normal angle $\theta = 89.5°$. In this case, wave instability is contributed mostly by the harmonic resonance with proton resonant energy ($E_{\parallel res}$) = 0, and $K_i$ can be expressed in an alternative form:

$$K_i \approx \int_0^\infty dv_\perp \left(W_\perp \frac{\partial f}{\partial v_\perp} + W_\parallel \frac{\partial f}{\partial v_\parallel}\right)\big|_{v_\parallel = 0}, \tag{B1}$$

where $W_\perp \equiv W_{m = m_\omega, \perp}$ and $W_\parallel \equiv W_{m = m_\omega, \parallel}$. Assuming the phase space density of energetic proton is symmetric about $v_\parallel = 0$, it follows that

$$\frac{\partial f}{\partial v_\parallel}\big|_{v_\parallel = 0} = 0, \tag{B2}$$

$$G_1\big|_{v_\parallel = 0} = \frac{\partial f}{\partial v_\perp}\big|_{v_\parallel = 0}, \tag{B3}$$

$$G_2\big|_{v_\parallel = 0} = 0. \tag{B4}$$

[37] Therefore

$$K_i \approx \int_0^\infty dv_\perp W_\perp \frac{\partial f}{\partial v_\perp}\big|_{v_\parallel = 0}, \tag{B5}$$

where $W_\perp$ is a function of $v_\perp$. It is straightforward to evaluate the $v_\perp$ dependence of $W_\perp$

$$W_\perp \propto x^2 (LJ_{m_\omega+1} - RJ_{m_\omega-1})^2 \propto x^2((m_\omega + 1)J_{m_\omega+1} + (m_\omega - 1)J_{m_\omega-1})^2, \tag{B6}$$

where $L/R = -(m_\omega + 1)/(m_\omega - 1)$ is used.

[38] For most of $m_\omega$ of interest, $5 \le m_\omega \le 40$, $(m_\omega + 1)/(m_\omega - 1) \approx 1$, and thus

$$W_\perp \propto x^2(J_{m_\omega+1}(x) + J_{m_\omega-1}(x))^2 = (2m_\omega)^2 J_{m_\omega}^2(x), \tag{B7}$$

which is consistent with *Horne et al.* [2000, and references therein].

[39] Peak value of $W_\perp$ is controlled by the Bessel function $J_{m_\omega}(k_\perp v_\perp/\Omega_{H^+})$. A numerical approximation for the peak

location of function $J_m^2(x)$ is $x_{\text{peak}} \approx 1.0304m + 1.6277$ for $m \geq 3$. Therefore

$$v_{\perp\text{peak}}^* = x_{\text{peak}}\Omega_{H^+}/k_\perp \approx \frac{x_{\text{peak}}}{m_\omega}\frac{\omega}{k_\perp}$$

$$= \frac{1.0304m_\omega + 1.6277}{m_\omega}\frac{\omega}{k_\perp}. \qquad (B8)$$

[40] The value of $k_\perp$ can be obtained from the cold plasma dispersion relation for MS waves at almost perpendicular propagation, $n^2 \approx RL/S$.

$$\omega/k \approx V_A\sqrt{\frac{\varepsilon(m_\omega+1)(m_\omega-1)}{(m_\omega\varepsilon+1)(m_\omega\varepsilon-1)} + 1 - \frac{(m_\omega+1)(m_\omega-1)}{(c/V_A)^2}}, \qquad (B9)$$

where $V_A$ is Alfvénic speed, $\epsilon$ is the ratio of electron to proton mass ($\sim 1/1840$), and $c$ is the speed of light.

## References

Ashour-Abdalla, M., and C. F. Kennel (1978), Nonconvective and convective electron cyclotron harmonic instabilities, *J. Geophys. Res.*, 83(A4), 1531–1543, doi:10.1029/JA083iA04p01531.

Boardsen, S. A., D. L. Gallagher, D. A. Gurnett, W. K. Peterson, and J. L. Green (1992), Funnel-shaped, low-frequency equatorial waves, *J. Geophys. Res.*, 97(A10), 14,967–14,976, doi:10.1029/92JA00827.

Bortnik, J., and R. M. Thorne (2010), Transit time scattering of energetic electrons due to equatorially confined magnetosonic waves, *J. Geophys. Res.*, 115, A07213, doi:10.1029/2010JA015283.

Chen, L., R. M. Thorne, V. K. Jordanova, C. Wang, M. Gkioulidou, L. Lyons, and R. B. Horne (2010), Global simulation of EMIC wave excitation during the 21 April 2001 storm from coupled RCM-RAM-HOTRAY modeling, *J. Geophys. Res.*, 115, A07209, doi:10.1029/2009JA015075.

Curtis, S. A., and C. S. Wu (1979), Gyroharmonic emissions induced by energetic ions in the equatorial plasmasphere, *J. Geophys. Res.*, 84(A6), 2597–2607, doi:10.1029/JA084iA06p02597.

Gkioulidou, M., C.-P. Wang, L. R. Lyons, and R. A. Wolf (2009), Formation of the Harang reversal and its dependence on plasma sheet conditions: Rice convection model simulations, *J. Geophys. Res.*, 114, A07204, doi:10.1029/2008JA013955.

Horne, R. B. (1989), Path-integrated growth of electrostatic waves: The generation of terrestrial myriametric radiation, *J. Geophys. Res.*, 94(A7), 8895–8909, doi:10.1029/JA094iA07p08895.

Horne, R. B., G. V. Wheeler, and H. S. C. K. Alleyne (2000), Proton and electron heating by radially propagating fast magnetosonic waves, *J. Geophys. Res.*, 105(A12), 27,597–27,610, doi:10.1029/2000JA000018.

Horne, R. B., R. M. Thorne, S. A. Glauert, J. M. Albert, N. P. Meredith, and R. R. Anderson (2005), Time scale for radiation belt electron acceleration by whistler mode chorus waves, *J. Geophys. Res.*, 110, A03225, doi:10.1029/2004JA010811.

Horne, R. B., R. M. Thorne, S. A. Glauert, N. P. Meredith, D. Pokhotelov, and O. Santolík (2007), Electron acceleration in the Van Allen radiation belts by fast magnetosonic waves, *Geophys. Res. Lett.*, 34, L17107, doi:10.1029/2007GL030267.

Jordanova, V. K., L. M. Kistler, J. U. Kozyra, G. V. Khazanov, and A. F. Nagy (1996), Collisional losses of ring current ions, *J. Geophys. Res.*, 101(A1), 111–126, doi:10.1029/95JA02000.

Jordanova, V. K., J. U. Kozyra, A. F. Nagy, and G. V. Khazanov (1997), Kinetic model of the ring current-atmosphere interactions, *J. Geophys. Res.*, 102(A7), 14,279–14,292, doi:10.1029/96JA03699.

Jordanova, V. K., C. J. Farrugia, R. M. Thorne, G. V. Khazanov, G. D. Reeves, and M. F. Thomsen (2001), Modeling ring current proton precipitation by electromagnetic ion cyclotron waves during the May 14–16, 1997, storm, *J. Geophys. Res.*, 106(A1), 7–22, doi:10.1029/2000JA002008.

Jordanova, V. K., Y. S. Miyoshi, S. Zaharia, M. F. Thomsen, G. D. Reeves, D. S. Evans, C. G. Mouikis, and J. F. Fennell (2006), Kinetic simulations of ring current evolution during the Geospace Environment Modeling challenge events, *J. Geophys. Res.*, 111, A11S10, doi:10.1029/2006JA011644.

Jordanova, V. K., R. M. Thorne, W. Li, and Y. Miashi (2010), Excitation of whistler-mode chorus from global ring current simulations, *J. Geophys. Res.*, 115, A00F10, doi:10.1029/2009JA014810.

Kasahara, Y., H. Kenmochi, and I. Kimura (1994), Propagation characteristics of the ELF emissions observed by the satellite Akebono in the magnetic equatorial region, *Radio Sci.*, 29(4), 751–767, doi:10.1029/94RS00445.

Kennel, C. (1966), Low-frequency whistler mode, *Phys. Fluids*, 9, 2190–2202, doi:10.1063/1.1761588.

Li, W., Y. Y. Shprits, and R. M. Thorne (2007), Dynamic evolution of energetic outer zone electrons due to wave-particle interactions during storms, *J. Geophys. Res.*, 112, A10220, doi:10.1029/2007JA012368.

Meredith, N. P., R. B. Horne, and R. R. Anderson (2008), Survey of magnetosonic waves and proton ring distributions in the Earth's inner magnetosphere, *J. Geophys. Res.*, 113, A06213, doi:10.1029/2007JA012975.

Němec, F., O. Santolík, K. Gereová, E. Macúšová, Y. de Conchy, and N. Cornilleau-Wehrlin (2005), Initial results of a survey of equatorial noise emissions observed by the Cluster spacecraft, *Planet. Space Sci.*, 53, 291–298, doi:10.1016/j.pss.2004.09.055.

Perraut, S., A. Roux, P. Robert, R. Gendrin, J. Sauvaud, J. Bosqued, G. Kremser, and A. Korth (1982), A systematic study of ULF waves above FH+ from GEOS 1 and 2 measurements and their relationships with proton ring distributions, *J. Geophys. Res.*, 87(A8), 6219–6236, doi:10.1029/JA087iA08p06219.

Rasmussen, C. E., S. M. Guiter, and S. G. Thomas (1993), A two-dimensional model of the plasmasphere—Refilling time constants, *Planet. Space Sci.*, 41, 35–43, doi:10.1016/0032-0633(93)90015-T.

Roeder, J. L., M. W. Chen, J. F. Fennell, and R. Friedel (2005), Empirical models of the low-energy plasma in the inner magnetosphere, *Space Weather*, 3, S12B06, doi:10.1029/2005SW000161.

Russell, C. T., R. E. Holzer, and E. J. Smith (1970), OGO 3 observations of ELF noise in the magnetosphere: 2. The nature of the equatorial noise, *J. Geophys. Res.*, 75(4), 755–768, doi:10.1029/JA075i004p00755.

Santolík, O., J. S. Pickett, D. A. Gurnett, M. Maksimovic, and N. Cornilleau-Wehrlin (2002), Spatiotemporal variability and propagation of equatorial noise observed by Cluster, *J. Geophys. Res.*, 107(A12), 1495, doi:10.1029/2001JA009159.

Toffoletto, F., S. Sazykin, R. Spiro, and R. Wolf (2003), Inner magnetospheric modeling with the Rice Convection Model, *Space Sci. Rev.*, 107(1–2), 175–196, doi:10.1023/A:1025532008047.

Tsyganenko, N. A. (1995), Modeling the Earth's magnetospheric magnetic field confined within a realistic magnetopause, *J. Geophys. Res.*, 100(A4), 5599–5612, doi:10.1029/94JA03193.

Tsyganenko, N. A. (1996), Effects of the solar wind conditions in the global magnetospheric configurations as deduced from data-based field models (Invited), in *International Conference on Substorms*, edited by E. J. Rolfe and B. Kaldeich, *Eur. Space Agency Spec. Publ., ESA SP-389*, 181–185.

Wang, C.-P., L. R. Lyons, T. Nagai, J. M. Weygand, and R. W. McEntire (2007), Sources, transport, and distributions of plasma sheet ions and electrons and dependences on interplanetary parameters under northward interplanetary magnetic field, *J. Geophys. Res.*, 112, A10224, doi:10.1029/2007JA012522.

Young, D. T., H. Balsiger, and J. Geiss (1982), Correlations of magnetospheric ion composition with geomagnetic and solar activity, *J. Geophys. Res.*, 87(A11), 9077–9096, doi:10.1029/JA087iA11p09077.

L. Chen and R. M. Thorne, Department of Atmospheric Sciences, University of California, 405 Hilgard Ave., Box 951565, 7127 Math Sciences Bldg., Los Angeles, CA 90095-1565, USA. (clj@atmos.ucla.edu)
R. B. Horne, British Antarctic Survey, Natural Environment Research Council, Madingley Road, Cambridge CB3 0ET, UK.
V. K. Jordanova, Los Alamos National Laboratory, MS D466, Los Alamos, NM 87545, USA.